FEATURE ARTICLE

A View from the Inside: Complexity in the Atomic Scale Ordering of Supported Metal Nanoparticles

Anatoly I. Frenkel,*[†,‡] Charles W. Hills,[§] and Ralph G. Nuzzo*[†,§]

School of Chemical Sciences and the Frederick Seitz Materials Research Laboratory, University of Illinois, Urbana, Illinois 61801, and Yeshiva University, 245 Lexington Avenue, New York, New York 10016

Received: July 18, 2001

In this report, we describe the use of several analytical techniques, including X-ray absorption spectroscopy (XAS), electron microscopy, and electron diffraction, as tools for characterizing the structural dynamics of supported Pt nanoscale particles. We examined several carbon-supported samples. Electron microscopy shows that the particles in these samples (S1−S3) have average particle diameters of roughly 20, 40, and 60 Å respectively, while electron microdiffraction data for these particles provided evidence of long-ranged ordering in the form of face centered cubic structures. This study highlights the use of advanced synchrotron X-ray absorption spectroscopies (XAS), in particular extended X-ray absorption fine structure (EXAFS) and X-ray absorption near-edge structure (XANES), as powerful tools for studying the structural habits and dynamics of these prototypical nanoscale materials. Using state-of-the-art methods of measurement and computational modeling, we demonstrate that it is possible to develop a detailed understanding of the shape and morphology of the nanoscale clusters. We use these techniques to provide information about the nature of their surface texturing, establishing that they preferentially adopt oblate ("hemispherical") cuboctahedra cluster shapes truncated along the [111] basal plane. We further describe the use of temperature-dependent EXAFS measurements to investigate the nature of bond relaxation phenomenon occurring within the small metallic nanoparticles. To evaluate these complex structural behaviors, the disorder parameters are calculated from temperature-dependent EXAFS data and then subsequently compared to simple molecular graphics simulations of mechanisms involving either full cluster or surface relaxations. The average bond length and static disorder obtained by experiment appear to best fit a model involving dominant contributions made by surface atom bond relaxation.

Introduction

An area of emerging importance in chemical research is the study of complex systems.[1] The ideas of complexity are perhaps best and most powerfully illustrated by the examples presented in biology. Living systems are adaptive[2−4] and demonstrate a hierarchical organization of structure and function manifested over many entangled length scales.[3−6] The assembly seen in these systems, one sensitively coupled to dissipative processes,[7] leverages patterns established by self-assembly[8] with structural organizations that result strictly on the basis of underlying dynamics.[7,8] It is not altogether surprising, given the sophistica-
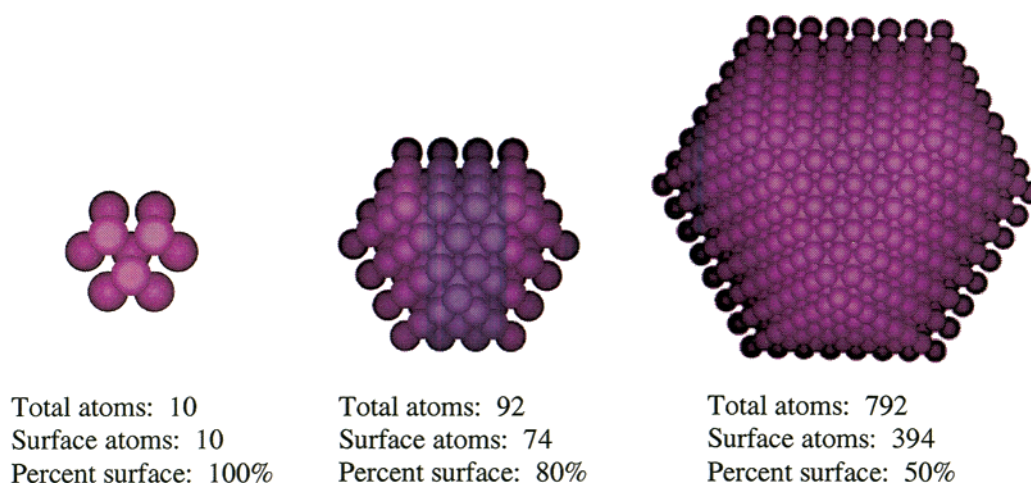
* Corresponding authors.
† Frederick Seitz Materials Research Laboratory, University of Illinois.
‡ Yeshiva University.
§ School of Chemical Sciences, University of Illinois.

SCHEME 1

Total atoms: 10
Surface atoms: 10
Percent surface: 100%

Total atoms: 92
Surface atoms: 74
Percent surface: 80%

Total atoms: 792
Surface atoms: 394
Percent surface: 50%

tion and beauty of these biologically derived inspirations, that the focus of research on complex chemical systems has come to rest on the structures and dynamics seen in extended systems (e.g., supramolecular assemblies,[9-11] biomimetic systems,[12-14] complex quantum systems,[15-18] and granular materials[19,20]). Such models might be taken to suggest that an implicit correlation exists between the size of an assembly and the degrees of freedom that might be embedded in its organization (with increasing possibilities for complex behavior following directly from this latter aspect).

In this report, we explore the issue of complexity in materials in a manner that, at first glance, appears to run directly counter to this notion. We consider the experimental challenges posed in the structural analysis of nanomaterials. The possibility that a nanoscale material system might be considered to be an example of a complex system arises from the significant perturbations that attend the finite scale of these systems. The properties of matter in bulk are frequently well understood and amenable to direct study. Diffraction, microscopy, or other relevant methods, for example, can directly establish an understanding of structure. Transformations follow pathways that can be described on the basis of simple thermochemical kinetic models. The electronic properties follow logically from the nature and bonding of the extended ensemble of atoms present. The finite size of nanoscale materials systems, however, leads to a number of perturbations that result in a wide range of nonbulklike behaviors. For example, the useful electronic and optical properties that originate from quantum confinement have received considerable attention in research and are now well appreciated.[21-29] The complex nature of the structural and chemical properties of these systems has only recently become the subject of increasingly detailed studies.[22-37] It is to a specific aspect of this latter interest that we address ourselves in this paper.

We consider in this feature article the structural characterization of supported metal nanoclusters. Such systems have unique properties that result from the very large fraction of the total number of atoms that reside either at or near their surface. A schematic depiction illustrating the scaling of "surface to bulk-like" atoms in a series of cuboctahedral clusters is shown to illustrate this size-related effect (Scheme 1). As is suggested by the numerous important reactions catalyzed by supported metal nanoclusters,[22,23,25,28-31,34,38-48] their unique, low coordination habits frequently dominate the properties seen in their reactivity. It seems obvious that reactions and interactions occurring at

the surfaces of nanoscale clusters could also lead to significant changes in structure that, in turn, might significantly impact the chemical properties of the system.[22,23,25,28-31,33-35,39,41,44,46-50] Such structural transformations, for all but the most specialized systems, remain very poorly understood.

In this report, we describe new approaches to the structural characterization of nanoscale metal clusters via the combined application of electron microscopy and extended X-ray absorption fine structure (EXAFS).[51] EXAFS is a spectroscopic technique that probes the local coordination environment of an atom; the inherent length scale of the measurement (the local environment can be probed within a radius ca. 8−10 Å from the central atom) corresponds well to the extent of metal−metal interactions and the number of coordination shells that might be formed in a cluster in the 1−2 nm size range. The basis of this spectroscopic measurement involves the analysis of the absorption coefficient of a metal atom in a cluster from ca. 40 eV to ca. 1500 eV past an absorption edge. The oscillatory behavior of the absorption coefficient in this region can be thought of as being caused by an interference that occurs between the outgoing and incoming photoelectron waves, which arises from the excitation of an electron from a core level to an unoccupied continuum state by absorption of a photon.[52] Given the formal scattering lengths associated with this effect, this interference signal contains information about the average atomic environment of an absorbing atom. The EXAFS experiment is both local, due to the short (∼10 Å) mean free path of the photoelectron, and essentially instantaneous, given that the core hole lifetime is only on the order of $10^{-16}-10^{-15}$ seconds. These factors make it an attractive technique for studying the structural dynamics of nanoparticles, materials whose finite size (as we develop in more detail below) ensures that no "true" long-ranged order can exist.

A series of notable articles has described the use of EXAFS to investigate the structures of supported metal particles.[53-64] An early publication detailing an analysis of the structures of supported Pt nanoparticles by EXAFS found a strong correlation between the measured first nearest neighbor (1NN) metal coordination number and the disorder of their bond lengths; lower coordination numbers appeared to correlate strongly with increased measured disorder in the first-shell metal−metal bond lengths.[54] These effects would be most sensitively seen in particles of the smallest size. The importance of anharmonic corrections to the 1NN pair interaction potential had yet to be appreciated in this pioneering work. Neglecting this effect leads

to a nonphysical decrease in 1NN bond lengths measured at high temperatures. Enhanced disorder in the 1NN bond distance was later correlated with the influences that result from cluster-support interactions.[59] These studies provide an important insight into the nature of supported metal nanoparticles, namely, that the bond lengths of surface atoms should exhibit enhanced structural disorder. Though the exact nature of these bonding environments remained unclear, these results demonstrated the potential of EXAFS for analyzing the distribution of atoms in the first coordination shell about selected atomic species, and they stimulated and supported further studies of the structures of bimetallic catalysts. The properties of bimetallic nanoparticles are of great interest in large part due to the improvements they yield in many industrial catalytic processes.[44] The structural dynamics of a binary phase can lead to an even larger degree of structural complexity in a nanoscale system, and it is noteworthy that these early investigations yielded intriguing suggestions about the importance of nonstatistical atomic distributions occurring within the particles.[56−58] These latter insights are ones that are unattainable through other experimental techniques.

A full understanding of the bonding habits present in metal nanoclusters, especially in terms of their dynamics and the disorder present in the metal−metal bonding, will greatly benefit the development of needed structure−property correlations for these systems. To properly employ EXAFS as an analytical tool towards this end requires one to account quantitatively for the anharmonic corrections that result from bond vibrations, since the latter explicitly define the coefficient of thermal expansion (and thus the temperature dependence of the bond lengths).[65,66] These corrections, which are described by a third cumulant in the pair distribution function,[67] contribute a negative term to the phase of the EXAFS oscillations. If this term is neglected, the nonlinear least-squares fit of the EXAFS data will show a nonphysical shortening of the bond lengths at elevated temperatures, since the anharmonicity of the interatomic potential becomes significant at this limit.

Determining the shape of supported clusters spectroscopically is also a complicated task for any one of several reasons. Free-standing, homogeneously grown metal particles typically adopt polyhedral shapes with varying degrees and types of truncation.[23] Given the difficulty associated with developing a deterministic model that can uniquely define both the shape and size of a cluster, EXAFS studies of supported nanoparticles typically assume, either implicitly or explicitly, that the particles adopt quasi-hemispherical shapes. The literature does describe notable studies that seek to determine both the average size and shape of supported metal nanoparticles.[68] As one example, an EXAFS analysis of Ir−Rh nanoparticles led to a proposed raft-like shape for these clusters.[61]

The issues involved in a spectroscopic analysis of an average particle shape or size are illustrated by the cluster models shown in Scheme 2. The two model particles shown are both characterized by a common average first-shell coordination number (here a value of ∼8 for a 92 atom hemispherical and an 55 atom spherical cuboctahedral cluster). At an elementary level of analysis (i.e., one limited to a first-shell fit to the EXAFS data), these distinct structural habits could not be uniquely differentiated. It also follows that the surface truncation system of the cluster would not be accessible to analysis in this way. High-resolution electron microscopy could help these analyses (for example, by differentiating between the ∼5 Å difference in size),[69,70] but most of the important microscopic structural properties would remain inaccessible to analysis.

SCHEME 2

[1NN] = 7.9   [1NN] = 8.2
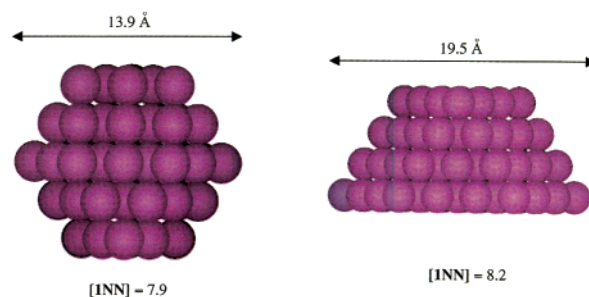
We focus our attention in this report on the development of an analytical approach to studying the structural phase dynamics of metal nanoparticles using a combination of real and *k*-space structural probes. We primarily focus in our discussion here on the application of EXAFS to this area of interest, detailing important modern advances that are enabling unprecedented new insights into the complex structural behavior seen in these systems.

With the development of ab initio theories,[71] programming codes that calculate theoretical scattering amplitudes and phase shifts in the EXAFS signal,[72] and data analysis packages (e.g., UWXAFS,[73] GNXAS,[74] and others[75]), the EXAFS technique has fully evolved into a quantitative spectroscopic tool for the structural analysis of nanoparticles. A key advantage of ab initio, multiple scattering EXAFS theories (e.g., FEFF[72]) is their ability to analyze distant coordination shells by explicitly including many-body contributions to the total absorption. Together with advanced data analysis techniques (e.g., FEFFIT), which estimate uncertainties in the results and implement multiple data set refinement with a nonlinear least-squares fit, these new capabilities now allow for a much more detailed analysis to be made of the local structures present around the absorbing atoms in a material. Perhaps no better critical test of this is available than that provided by the analysis of distant coordination shells (the modeling of which requires explicit consideration of contributions that arise from multiple scattering interactions). In close-packed crystal structures, the number of scattering paths that might contribute in this way in principle can be quite large. Fortunately, in systems with high symmetry, only those multiple-scattering contributions that lie along collinear directions are most significant.[76−78] This fact reduces the complexity of the analysis in high-symmetry systems and has leveraged the types of analyses that EXAFS can be used to address. For example, a correct understanding of multiple scattering effects was instrumental in using EXAFS to measure the bond angles exhibited in binary alloys.[79,80]

Coupled with advances in theory and data analysis, corresponding developments in X-ray beamline optics, as well as the availability of high intensity synchrotron X-ray sources, have opened entirely new possibilities for measuring EXAFS data on dispersed nanoparticles with unprecedented spatial resolution (essentially analogous to that possible for bulk). Since the spatial resolution of the EXAFS measurement (the ability to resolve the fine details embedded in the pair distribution function of the nearest neighbor atoms, e.g., unimodal vs bimodal distribution) is inversely proportional to the maximum photoelectron wavenumber, it is limited by experimental noise at high *k*. Instrumental advances have greatly improved the useful *k*-range of most EXAFS measurements, and therefore, higher accuracy can be achieved in deducing the structural parameters of interest in a nanoscale material system.

In this Article, we describe state-of-the-art experimental and theoretical tools that we have used to analyze structures in a

prototypical metal nanoparticle system. Specifically, we characterize the structure of a series of carbon supported Pt nanoparticles, ones with different average cluster sizes. The average particle sizes were determined by scanning transmission electron microscopy (STEM), and the nature of their close-packed structures was established by electron microdiffraction. The X-ray absorption spectroscopy experiments were performed at the National Synchrotron Light Source at Brookhaven National Laboratory (UIUC/Lucent beamline X16C). These data establish in an unambiguous way the complex nature of the atomic scale ordering and bonding found in these nanoscale clusters. A number of new structural understandings are established in this work. These include the nature of the crystal stacking biases established by the particle growth and the characteristic distributions of the bond relaxation embedded in the cluster.

Experimental Section

High-Resolution Scanning Transmission Electron Microscopy. Microscopy studies were carried out using a field emission, Vacuum Generators HB501 STEM operated at 100 kV. The specimens were prepared by dipping a copper mesh supported, holey carbon grid (SPI Supplies) into the three samples: 10%, 40%, and 60% (by weight) Pt supported on Vulcan XC-72 carbon black (ETEK, Inc.). Digital-micrograph (Gatan) digital-video data-acquisition software was used to gather images and perform the analysis. The particle sizes were determined by measuring the full-width half-maximum (fwhm) of the cross section intensity profiles of individual nanoparticles.

Electron Microdiffraction. The ordered microstructure of the nanoparticles was probed by electron microdiffraction. The specimens were prepared in a similar manner as those used in the microscopy study, except copper mesh, holey carbon grids with supported silicon crystals were used to support the samples. An incident electron beam probe was focused on the nanoparticles of interest, and the diffracted electrons were collected on a phosphor screen. Due to the fact that the diffraction patterns for individual nanoparticles degrade during the exposure to the electron beam, the diffraction images were gathered promptly. A low-light level television camera was used to gather these data and Scion Image (NIH/Scion Corp.) software was used to capture the images. Digital Microscopist software was used to analyze the patterns, using the diffraction patterns from the silicon crystals to calibrate the camera constant.

X-ray Absorption Spectroscopy. All X-ray absorption data were measured at the UIUC/Lucent beamline X16C at the National Synchrotron Light Source, located at the Brookhaven National Laboratory in Upton, NY. The intensity of the incident beam (I_0) was measured with a 15 cm long ion chamber filled with a 10:1 mixture of He:Ar. X-ray absorption data from the sample were measured in transmission mode by scanning from 200 eV below to 1700 eV above the Pt L_3 edge. A 30 cm long Ar filled ion chamber placed after the sample (collinear with the beam direction) was used to measure I_1. A thin sample of Pt metal foil was used to calibrate the X-ray energy during each scan. The calibration measurement was made with a third, 30 cm long Ar filled ion chamber (I_2) placed after I_1. The position of the metal absorption edge (Pt, 11564 eV) could then be determined by placing the Pt metal standard between ion chambers I_1 and I_2 and measuring the absorption coefficient in the metal standard.

To collect in-situ X-ray absorption data from the carbon supported Pt particles, about 25 mg of sample was pressed at

~5 tons into a rectangular wafer (ca. 1.5 × 1 cm) using a hydraulic pellet press. To avoid thickness effects (i.e., self-absorption),[81] the pellets were formed with a thickness, x, of 0.5 mm, satisfying the condition that the absorption edge steps $\Delta\mu x \leq 1$ at both the Pt L_3 and Ru K absorption edges. The wafer was then loaded into a custom designed and built catalyst cell that allows simultaneous in-situ X-ray fluorescence and transmission measurements over an operating temperature range of 150 to 773 K.

The in-situ cell was purged with H_2 for 1 h after loading the sample wafer. The temperature was monitored with a chromel/alumel thermocouple (Omega) mounted directly on the sample mounting stage. To activate the samples, each was heated to a temperature of 673 K and held at that limit for 1 h. The samples were then cooled in the high-purity H_2 atmosphere to room temperature before making the EXAFS measurements.

EXAFS Analysis. The X-ray absorption data were analyzed using the UWXAFS analysis package.[73] The analysis was performed using the following general procedure: (1) the smooth, isolated-atom background function was removed from the experimental X-ray absorption coefficient data; (2) theoretical photoelectron scattering amplitudes and phase shifts were calculated for a model structure; and (3) the theoretical EXAFS signal was fit to the experimental EXAFS data in r-space by Fourier transforming both the theoretical and experimental data.

For each measured X-ray absorption spectrum, the AUTOBK code[82] was used to normalize the absorption coefficient, $\mu(k)$, and separate the EXAFS, $\chi(k)$, from the isolated atom absorption background, $\mu_0(k)$. This process is shown in the following relation:

$$\chi(k) = \frac{\mu(k) - \mu_0(k)}{\Delta\mu_0(k)} \qquad (1)$$

where k is the photoelectron wavenumber, $k = \sqrt{2m(E - E_0)}/\hbar^2$, E is the photon energy, and E_0 is the photoelectron energy origin (chosen at the middle of the absorption edge jump). The background function, $\mu_0(k)$, was obtained by minimizing the signal in the low-r region of the Fourier transformed $\chi(k)$ data.

The EXAFS signal, $\chi(k)$, which is the sum of all contributions, $\chi_i(k)$, from groups of atoms that lie at approximately equal distances from the absorbing atom (i.e., the ith shell) was adjusted by applying the EXAFS equation, written in the following extended form:[72]

$$\chi(k) = \sum_i \frac{S_0^2 N_i}{kR_i^2} |f_i^{\text{eff}}(k)| \sin\left[2kR_i - \frac{4}{3}\sigma_i^{(3)}k^3 + \delta_i(k)\right] e^{-2\sigma_i^2 k^2} e^{-2R/\lambda_i(k)}$$

$$(2)$$

where k is the photoelectron wavenumber, $f_i^{\text{eff}}(k)$ and $\delta_i(k)$ are the photoelectron scattering-path amplitude and phase, respectively, S_0^2 is the passive electron reduction factor, R_i is the effective half-path-length (which is equal to the interatomic distance for single-scattering paths), σ_i^2 (discussed further below) is the mean-square deviation in R_i, $\sigma_i^{(3)}$ is the third cumulant, and $\lambda_i(k)$ is the photoelectron mean free path. The computer code FEFFIT was used to fit theoretical EXAFS calculated with FEFF6 to the experimental $\chi(k)$ data. In this procedure, FEFF6 was used to calculate the photoelectron scattering-path amplitudes, $f_i^{\text{eff}}(k)$, and phases, $\delta_i(k)$, for the absorbing atom in a specific model structure.
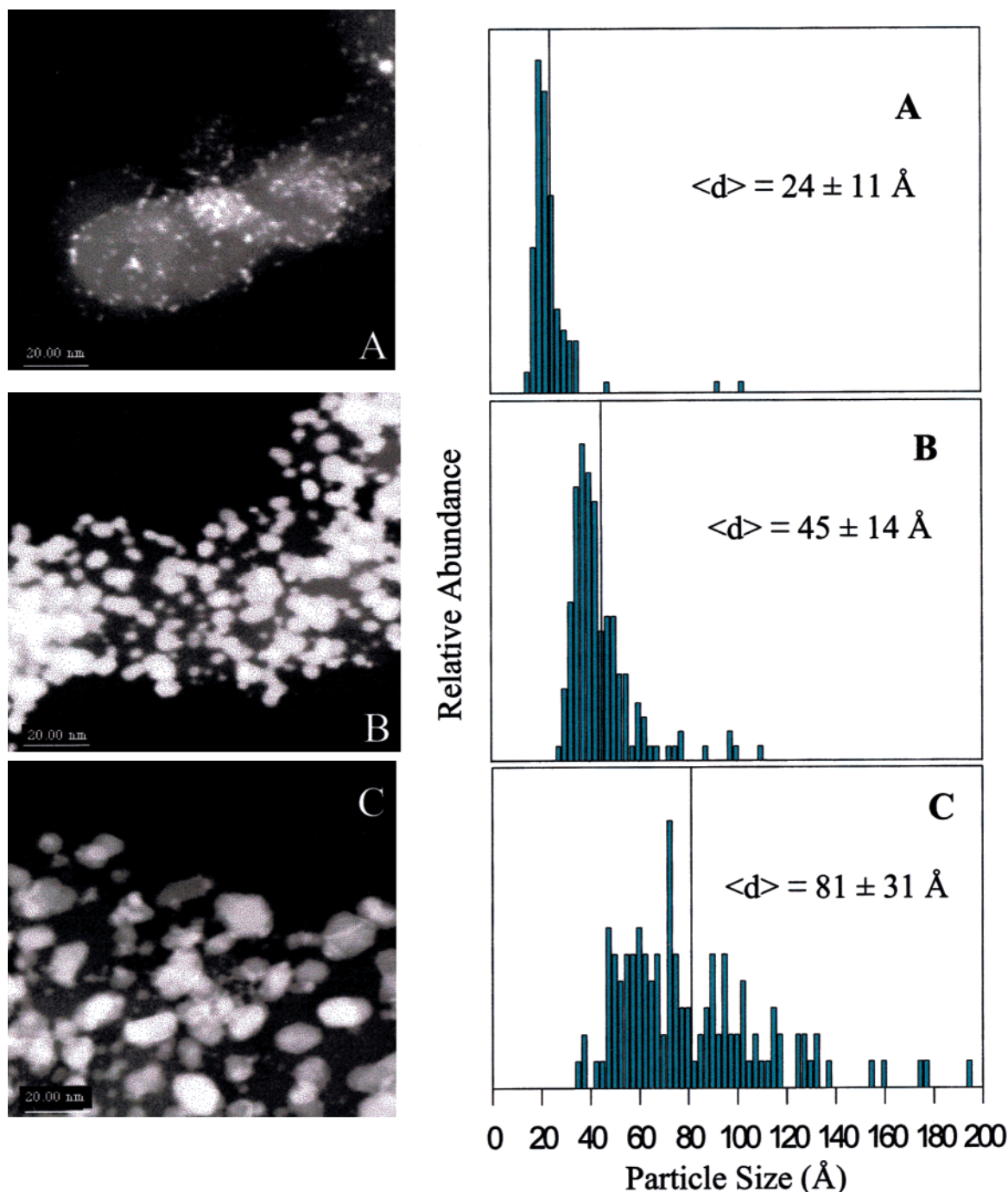
Feature Article

J. Phys. Chem. B, Vol. 105, No. 51, 2001 **12693**

Figure 1. Representative dark field STEM micrographs of samples S1 (A), S2 (B), and S3 (C). Next to each micrograph is the representative particle size distribution for each sample (S1 (A), S2 (B), and S3 (C)).

The mean-square deviation, σ^2, of the first nearest neighbor (1NN) distance can be represented to a good approximation as a superposition of static (σ_s^2) and dynamic (σ_d^2) terms:

$$\sigma^2 = \langle (r - \langle r \rangle)^2 \rangle = \sigma_s^2 + \sigma_d^2 \qquad (3)$$

To separate the temperature-independent σ_s^2 and temperature-dependent σ_d^2, one can use a simple correlated Einstein model[83] for σ_d^2:

$$\sigma_d^2 = \frac{\hbar}{2\omega\mu} \frac{1 + \exp(-\Theta_E/T)}{1 - \exp(-\Theta_E/T)} \qquad (4)$$

where ω is a bond vibration frequency, μ is the reduced mass

of the 1NN atomic pair, and $\Theta_E = \hbar\omega/k_B$ is the Einstein temperature. Thus, the total σ^2 in this approximation depends on three parameters: T, Θ_E, and σ_s^2. By replacing the total σ^2 in eq 2 by a sum of the dynamic and static terms (eq 3), the best fit results for Θ_E and σ_s^2 can be obtained from a concurrent nonlinear least-squares fitting of eq 2 to the EXAFS data taken (in this study) at four discrete temperatures.

Results and Discussion

Electron Microscopy and Microdiffraction. Figure 1 shows representative dark-field micrographs of the three Pt on carbon samples used in this study, along with the particle size distributions measured for each. The sample preparation differed only in the weight loading of the Pt used to form the particles.
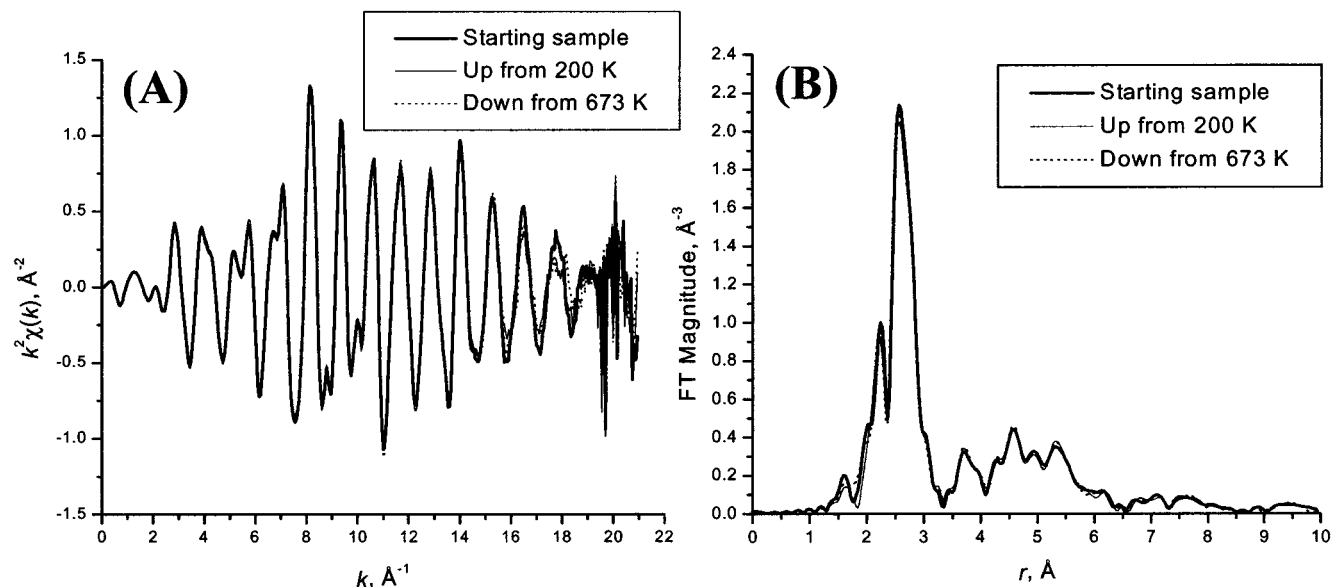
Figure 2. Representative microdiffraction images (A, C, and E) measured from individual particles in sample S1. The diffraction patterns were indexed to fcc structures as shown in panels B, D, and F, respectively.

TABLE 1: Sample Legends, Average Particle Sizes, and Standard Deviations, as Obtained by STEM

	S1	S2	S3
Pt/C, %	10	40	60
$\langle d \rangle$, Å	24 ± 11	45 ± 14	81 ± 31

As the figure indicates, the average particle size (and the polydispersity of the sample) increases with increasing Pt content. For sample S1 (Figure 1A, 10% Pt/C), the majority of particles fall in a narrow range around the measured average particle size of ca. 24 Å. The particles for sample S2 (Figure 1B, 40% Pt/C) are somewhat larger on average, and the particles in sample S3 (Figure 1C, 60% Pt/C) have a broad range of sizes centered on an average particle dimension of ca. 81 Å. The average particle sizes for all the samples are listed in Table 1.

Strong electron microdiffraction was seen from all of the Pt nanocrystal samples. Figure 2A,C,E presents representative diffraction patterns measured on sample S1 (10% Pt/C) corresponding to clusters of ca. 20 Å in diameter. These diffraction patterns can be uniquely indexed to a simple close-packed face

centered cubic (fcc) structure as shown in Figure 2B,D,F. These data confirm that there is an ordering of the atomic microstructure present within these crystals.

Visual Examination of the EXAFS Data. To ensure reproducibility and test for thermal hysteresis in the X-ray spectra, the samples were activated by heating to 400 K in an H_2 environment before measuring the EXAFS data. Data sets were then measured at 300 K before and after each thermal treatment and compared for all the samples. As shown in Figure 3A, the data measured for the reduced sample at various points during the temperature ramp were indistinguishable, to within the experimental noise level, in both amplitude and phase. This unambiguously establishes that all the samples were stable and that no coalescence of particles occurs over the ranges used in the temperature-dependent measurements described below. This reproducibility test can also be visualized in r-space by carrying out a Fourier transform over a k-range extending from 2 and 16 Å^{-1} (shown in Figure 3B). Of particular note in this latter data is the absence of a low-r signal (below ca. 2 Å). The

Feature Article

J. Phys. Chem. B, Vol. 105, No. 51, 2001 **12695**

Figure 3. (A) Representative reproducibility test in k-space. k^2-weighted EXAFS measurements for S2 were made at 300 K before any thermal treatment ("starting sample"), after cooling to 200 K and then heating to 300 K ("up from 200 K"), and after heating to 673 K and then cooling to 300 K ("down from 673 K"). H_2 was flowing continuously during all temperature ramps. (B) Representative reproducibility test in r-space. Shown are the FT magnitudes of the k^2-weighted EXAFS data in panel A.
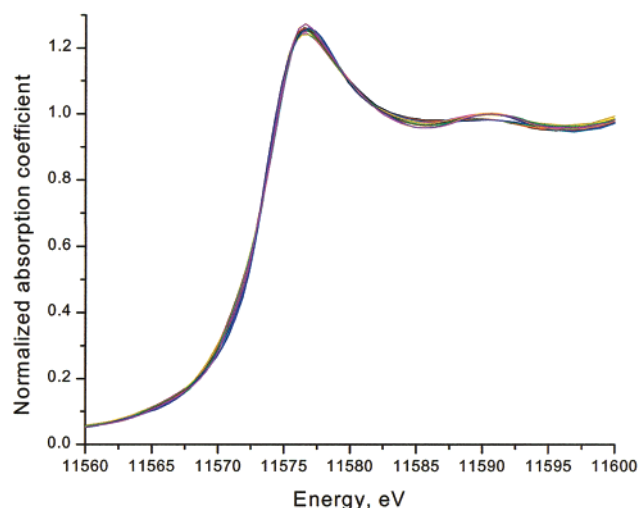
Figure 4. XANES region in samples S1, S2, S3, and Pt foil at 200, 300, 473, and 673 K. Sixteen measurements are shown.

sensitivity of EXAFS to the presence of low-Z neighbors due to contaminants (e.g., oxygen due to the surface oxidation of the cluster) is remarkably good and the data are thus strongly suggestive of a fully reduced ensemble of metal particles.[51] This latter observation is also consistent with the XANES results (Figure 4), which indicates that the particles are ones with a metallic density of states at the Fermi surface.

More information about the size and temperature sensitivities of the Pt particles' structures can be obtained by visually examining the background-subtracted EXAFS data and their Fourier transforms in r-space. Figure 5A shows representative $\chi(k)$ data for clusters differing in their average size. These data demonstrate a universal trend; as the average particle size decreases, the signal intensity is reduced throughout the entire k-range. This behavior is consistent with a decrease in coordination number, N_i, in each shell since the intensity of the EXAFS oscillations is proportional to the average number of scatterers surrounding the central atom. Since the thermal factor (the Debye–Waller factor in eq 2) for all samples should be similar

at each temperature, one expects that the reduction in intensity observed between different samples should be independent of k, an inference that is consistent with the behaviors demonstrated in Figure 5A.

Figure 5B shows the Fourier transforms of the $\chi(k)$ data shown in Figure 5A. The peak positions are shifted in this pseudoradial structure function to shorter distances relative to those expected for the true interatomic distances, due to extra terms that contribute to the phase of the EXAFS oscillations (eq 1, the phase-corrected bonding distances seen in these clusters are discussed below).[66,67] The strong peak between 2 and 3 Å corresponds to the interaction occurring between the 1NN platinum atoms. The amplitude of the peak is the highest for the Pt foil and decreases gradually from sample S3 to sample S1. This intensity reduction is predominantly caused by the decrease in the average 1NN coordination number that results from the changing ratio of surface to bulklike atoms in the clusters (see below). The signal at higher distances (between 3 and 6.5 Å) is a superposition of the single-scattering photoelectron paths from the more distant nearest neighbor shells and the contributions arising from multiple scattering. As we shall show, the details of the EXAFS spectrum in this range carry a unique signature of the underlying atomic arrangements, one remarkably sensitive to fine details of the atomic ordering. The similarities of the spectra in this distance range, as shown in Figure 5B, suggests that (to first-order) the local structure in the nanoparticles is isostructural to that in bulk Pt metal.

Figure 6A presents the temperature-dependent $\chi(k)$ data set measured for the S2 Pt/C sample. Corresponding data for the S1 and S3 samples are given in the supporting materials. A number of striking changes are evidenced in these data, but one especially stands out even on casual inspection. The magnitude of the temperature sensitivity is most clearly illustrated by examining the changes in EXAFS amplitude seen across the entire range. Naturally, the low-k portion of the spectra is nearly unaffected by an increase in temperature, whereas the intensity seen in the high-k range is greatly reduced. These effects are governed by the Debye–Waller factor term, $e^{-2\sigma^2 k^2}$, that is functionally dependent on both k and temperature (eqs 2–4).
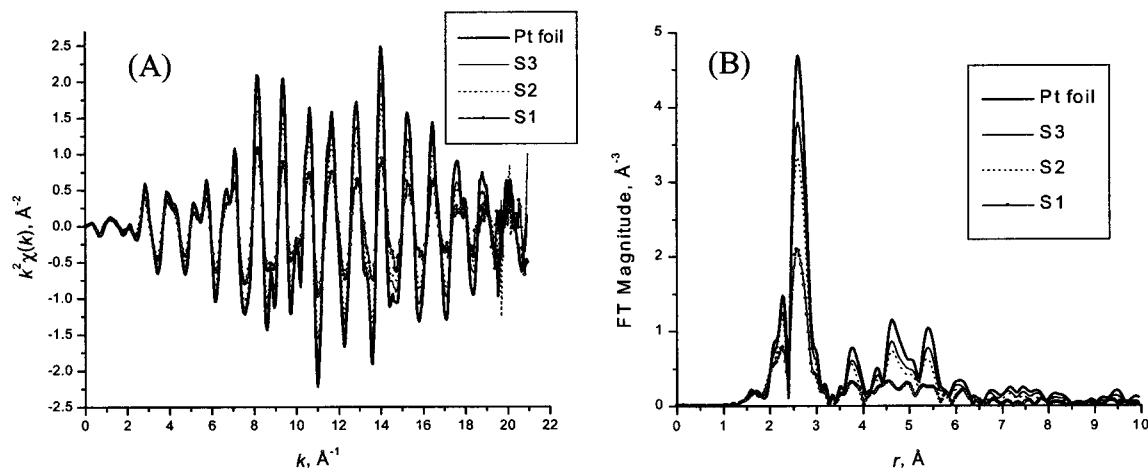
Figure 5. Size-dependent changes in the nanoparticles. Representative k^2-weighted EXAFS data (A and B) for samples S1, S2, S3, and Pt foil at 200 K.
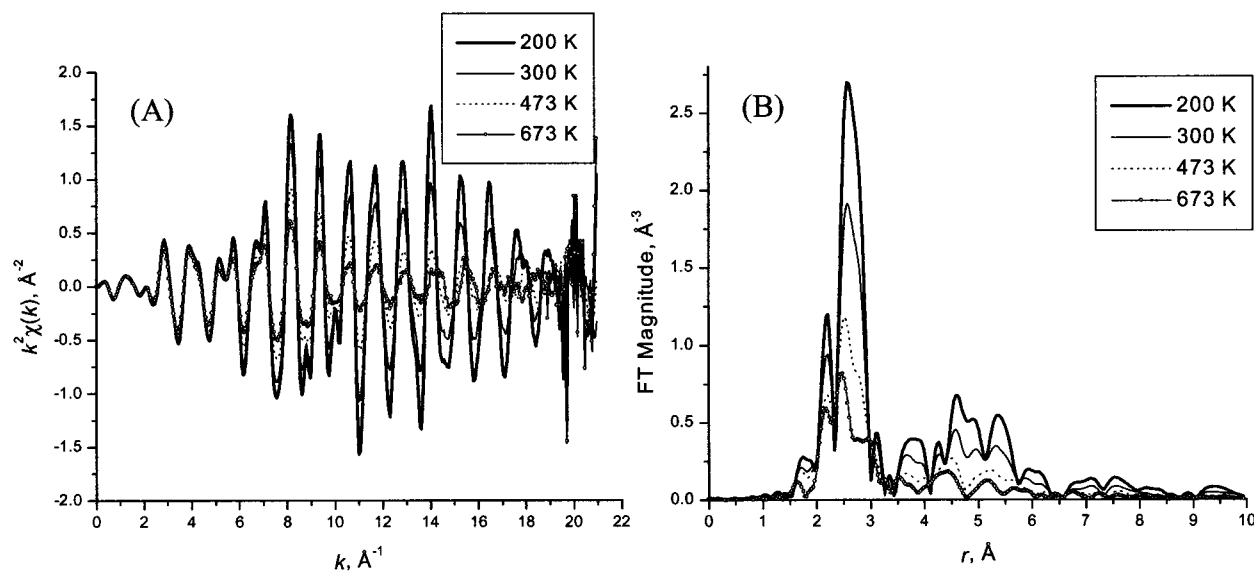

Figure 6. Temperature-dependent changes in the EXAFS data for carbon-supported Pt nanoparticles. Representative k^2-weighted EXAFS (A) and Fourier transform EXAFS data (B) of sample S2 at the temperatures 200, 300, 473, and 673 K.

Figure 6B displays the Fourier transform of the k-space data shown in Figure 6A. The temperature effects seen in the k-space data are more clearly illustrated here. One also sees that, as temperature increases, the position of the 1NN peak (between 2 and 3 Å) shifts toward smaller values. The latter effect is caused by the important contributions made by the anharmonicity of the effective pair interaction potential (as embodied by the third cumulant, $\sigma_i^{(3)}$), which is strongly temperature-dependent.[83] Ignoring this factor during the EXAFS data analysis would lead one to presume that a nonphysical shortening of the bond length occurs at elevated temperatures.[67]

The discussion above illuminates a number of important qualitative ideas about the structures of the Pt nanoparticles. First, the particles are metallic structures, ones with habits and bonding environments similar to those found in the bulk. Second, the system shows a strong sensitivity to temperature, with the disorder in the bonding increasing markedly and monotonically with the temperature. In the sections that follow, we describe a full quantitative analysis of the EXAFS data, one that extends these notions and develops detailed insights into the structural dynamics of this system.

First-Shell Analysis of the Temperature-Dependent EXAFS Data. We begin with an analysis that provides a basis

TABLE 2: Einstein Temperatures and Static Disorder Obtained by Concurrent Analysis of the First-Shell Data Measured at Different Temperatures

	S1	S2	S3	Pt foil
Θ_E, K	192(4)	197(5)	194(3)	190(2)
static σ^2, Å^2	0.0017(2)	0.0010(2)	0.0009(1)	0.0005(1)

for interpreting the distributions of metal−metal bonding distances present in a nanoparticle, including a detailed assessment of the characteristic disorder of the system as defined by the Debye−Waller factor, σ^2. The concurrent analysis of the temperature-dependent EXAFS data provides a reliable way to do this by quantitatively breaking the correlation between σ^2 and S_0^2 (the passive electron factor that accounts for final state relaxation effects, eq 2). Even though these two variables make different contributions to the EXAFS equation, they both reduce the amplitude of the EXAFS oscillations. The reliability of this procedure can be tested by comparing the experimental and literature values of Pt's Debye temperature, Θ_D. Using the Pt foil EXAFS data analysis (Table 2), the fit yields a value for $\Theta_E = 190$ K; this can be used to estimate a Debye temperature through the approximation $\Theta_D = (4/3) \Theta_E$, which is valid for metals with fcc or bcc structures.[66] The latter assumption that the Pt atoms adopt fcc packing in the clusters is, as we have

Feature Article

J. Phys. Chem. B, Vol. 105, No. 51, 2001 **12697**

TABLE 3: 1NN Distances Obtained by the Concurrent Analysis of the First-Shell Data Measured at Different Temperatures

T, K	S1	S2	S3	Pt foil
200	2.753(4)	2.761(7)	2.761(3)	2.761(2)
300	2.756(3)	2.762(3)	2.763(2)	2.762(3)
473	2.759(5)	2.771(5)	2.770(3)	2.771(4)
673	2.763(6)	2.775(7)	2.777(6)	2.779(5)

shown, strongly supported by the STEM data. The Debye temperature estimated by this approximation is 253 K, which is in good agreement with the literature value of 240 K.[84] This establishes that the value of S_0^2 obtained from the data on the bulk sample is reliable. The measured value of $S_0^2 = 0.84(2)$ is then held fixed for all the other data, since it is a property of only the absorbing atom.

The temperature-dependent 1NN distances obtained in the simultaneous fits to the first-shell data for the bulk Pt sample and the series of size-varying carbon-supported nanoparticles are given in Table 3.

Multiple-Scattering Analysis of the EXAFS Data. Equation 2 can now be used to analyze the entire EXAFS spectrum in a way that implicitly includes the contributions from multiple-scattering paths. A finite number of photoelectron paths were found to be the ones most important for allowing an adequate description of the EXAFS data through 6.2 Å for the system of interest here (an fcc structure with a lattice parameter of 3.92 Å). The high-symmetry paths of concern include the following: five single-scattering (SS1−SS5) paths from the central (absorbing) Pt^0 atom to its neighbors in the 1st through 5th shells; three triangular scattering paths, TR1-TR3; and two collinear focusing double (DS) and triple-scattering (TS) paths (Table 4 and Figure 7).

In the fits, the photoelectron energy origin correction, ΔE_0, was set to be the same for all paths. The half path lengths, R, were not varied independently for different paths, since they all must be related to the cluster lattice parameter. Since the
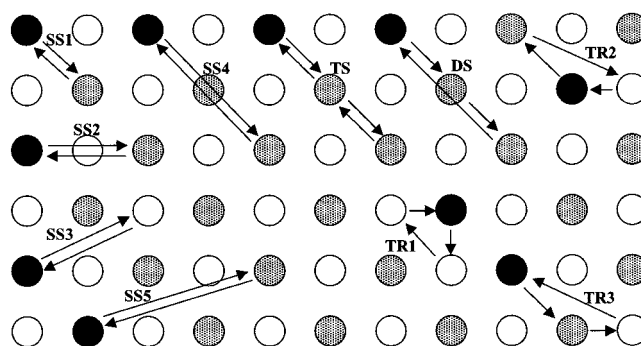

Figure 7. Schematic representation of all the paths used for EXAFS data analysis. The Pt fcc structure is shown: the out of plane atoms are denoted by empty circles; the in plane atoms are shaded. Black circles denote absorbing (central) atoms. The TR3 and the DS paths have analogous, time-reversed configurations (not shown) for which the direction of the electron propagation is reversed.

lattice parameter may vary for different cluster sizes (a relaxation effect that has been described in the literature),[23,85−91] a universal distortion parameter, the isotropic lattice expansion factor ϵ, was introduced through the following relationship: $R_i = (\epsilon + 1)R_i^{(m)}$, where $R_i^{(m)}$ is the half length predicted by fcc space group rules for all possible linkages between the atoms on the basis of the lattice parameter chosen for the FEFF model (3.92 Å). The value of ϵ was varied identically for all paths in the fits.

The path degeneracies, N, (which are equal to the coordination numbers for the single scattering paths) and the bond length disorders, σ^2, were varied independently for most paths; however, due to the similarity of the geometries of the TR2 and TR3 paths, the σ^2 of the TR3 path was constrained to be the same as that of the TR2 path (Table 5). Since the shape of the nanoclusters had been established by TEM to be a hemispherical (i.e., oblate shape), the degeneracies and σ^2 of the DS and TS paths were constrained to vary in accordance

TABLE 4: List of All Photoelectron Paths Used for Modelling EXAFS Data of Pt Foil and the Nanoclusters[a]

path	description	$R^{(m)}$, Å	$N^{(m)}$	N	σ^2
SS1	$Pt^0 \xrightarrow{1NN} Pt^1 (180°) \xrightarrow{1NN} Pt^0$	2.772	12	v	v
SS2	$Pt^0 \xrightarrow{2NN} Pt^2 (180°) \xrightarrow{2NN} Pt^0$	3.920	6	v	v
TR1	$Pt^0 \xrightarrow{1NN} Pt^1 (120°) \xrightarrow{1NN} Pt^1 (120°) \xrightarrow{1NN} Pt^0$	4.158	48	v	v
SS3	$Pt^0 \xrightarrow{3NN} Pt^3 (180°) \xrightarrow{3NN} Pt^0$	4.801	24	v	v
TR2	$Pt^0 \xrightarrow{1NN} Pt^1 (150°) \xrightarrow{3NN} Pt^1 (150°) \xrightarrow{1NN} Pt^0$	5.172	48	N_{TR1}	v
TR3	$Pt^0 \xrightarrow{3NN} Pt^3 (150°) \xrightarrow{1NN} Pt^1 (60°) \xrightarrow{1NN} Pt^0$	5.172	96	$2N_{TR1}$	σ_{TR2}^2
SS4	$Pt^0 \xrightarrow{4NN} Pt^4 (180°) \xrightarrow{4NN} Pt^0$	5.544	12	v	v
DS	$Pt^0 \xrightarrow{1NN} Pt^1 (0°) \xrightarrow{1NN} Pt^4 (180°) \xrightarrow{4NN} Pt^0$	5.544	24	$2N_{SS4}$	σ_{SS4}^2
TS	$Pt^0 \xrightarrow{1NN} Pt^1 (0°) \xrightarrow{1NN} Pt^4 (180°) \xrightarrow{1NN} Pt^1 (0°) \xrightarrow{1NN} Pt^0$	5.544	12	N_{SS4}	σ_{SS4}^2
SS5	$Pt^0 \xrightarrow{5NN} Pt^5 (180°) \xrightarrow{5NN} Pt^0$	6.198	24	v	σ_{SS4}^2

[a] The superscript in the path description denotes the coordination shell around the central atom Pt^0, the number in parentheses is the scattering angle, and the label under the arrow connecting two adjacent scattering atoms indicates the distance between them. The paths geometries are visualized in Figure 10. The model half path lengths and degeneracies were used as an input for FEFF calculations for the fcc structure with a_{model} = 3.92 Å. The last two columns specify whether the fitting parameters N and σ^2 were varied or constrained while fitting FEFF theory to the data.

TABLE 5: Average Coordination Numbers N_i for the Pairs Including the Central Atom and Its *i*th (from 1 to 5) nearest Neighbors, Obtained from the Multiple-Scattering Analysis of the 200 K Data in All Samples[a]

i	S1	S2	S3	Pt foil	bulk fcc
1	8.3(5)	10.5(5)	11.4(6)	12.6(7)	12
2	2.3(1.1)	4.0(1.3)	4.7(1.7)	5.9(2.0)	6
3	10.9(3.2)	16.8(3.5)	19(4)	23(5)	24
4	5.5(1.4)	7.6(1.4)	8.5(1.6)	11(2)	12
5	5.4(3.4)	10(4)	11(4)	14(5)	24

[a] Coordination numbers in bulk fcc symmetry are given for comparison.

with that of the SS4 path.[78] Similarly, the degeneracies of the TR2 and TR3 paths were related to that of the TR1 path in the fit (Table 5). Finally, the third cumulant, $\sigma^{(3)}$, was added to the list of variables for the 1NN path to account for the temperature-dependent and, possibly, size-dependent asymmetry of the 1NN pair distance distribution function.

Figure 8 presents the theoretical EXAFS fits of the data collected for all the samples and the Pt metal foil at 200 K. The fit results for the coordination numbers of the nearest neighboring shells, first through the fifth, are summarized in the Table 5.

Modeling the Nanoparticle Size and Shape. For particles with diameters smaller than 30–50 Å, the coordination number is a strong and nonlinear function of the particle diameter (Scheme 3). This property has been widely used in EXAFS analysis to determine the size of nanoparticles.[55,68] A first-shell analysis cannot unambiguously provide for an understanding of the coordination numbers and mean square disorder in the 1NN bond lengths due to their correlation with other fitting parameters as well as the model dependence of the analysis procedure. For these reasons, the first-shell coordination numbers, in and of themselves, cannot be interpreted in a strict quantitative structural sense. Indeed, if all other conditions (e.g., size of the cluster, symmetry of atomic packing, and the lattice parameter) are held equal, the two limiting cluster forms—one spherical and the other hemispherical—will have different average coordination numbers. The latter cluster will have the smaller coordination number since it has a larger contribution from surface-truncated bonds than does the former (Scheme 2). In addition, a subtle effect, the variety of possible cluster surface orientations, further complicates the cluster size determination (as will be shown below).

It has been demonstrated, on the basis of a simple calculation of the size-dependence of the first four coordination numbers in a hemispherical fcc cluster, that the particle size effect on the coordination number is much more strongly manifested for more distant shells (i.e., scattering paths that have a higher probability of effectively "sampling" the cluster exterior).[92] This result, in conjunction with similar results from model calculations,[68,93] suggests that the reliability of a spectroscopy-based particle size determination would be increased if the coordination numbers from higher shells were obtained. This, though, would really provide no understanding that could not be more directly obtained from STEM data. The multiple-shell analyses are a much richer source of information than this, however. Indeed, using the entire set of coordination numbers in conjunction with their uncertainties provides information possessing much greater structural depth—reporting about the shape, size, and morphologies of the nanoclusters. We turn now to a consideration of these points.

Due to differences in the geometry of clusters with different sizes, shapes or lattice symmetries, each cluster must generate
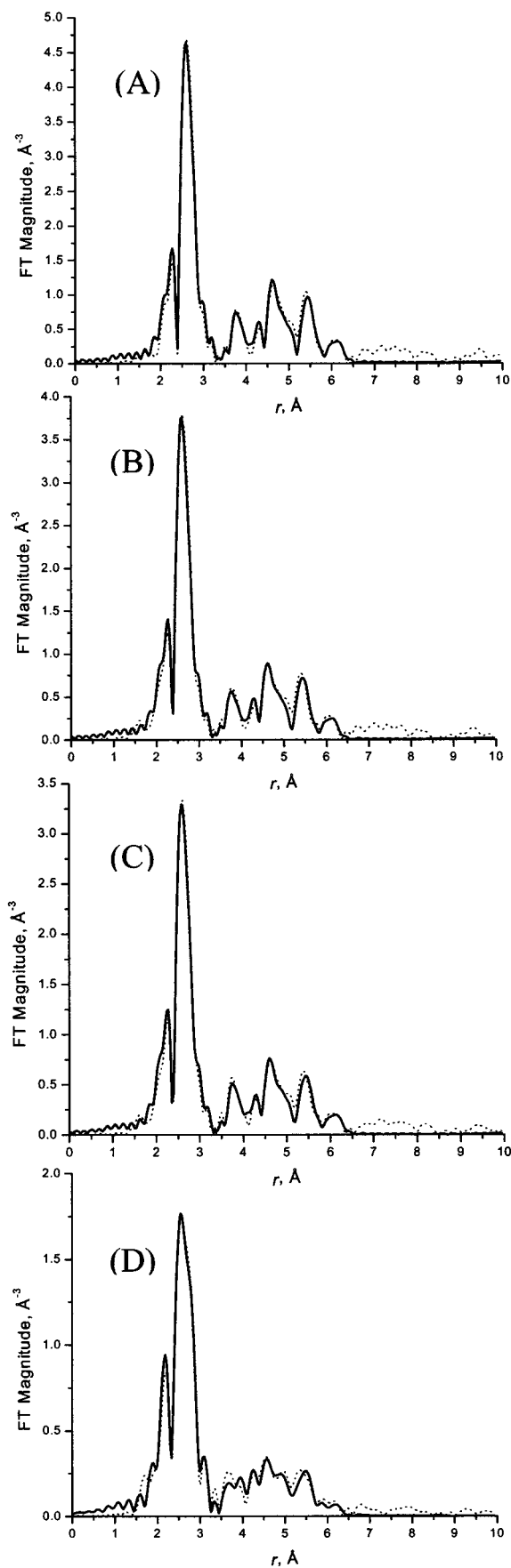

Figure 8. FT magnitudes of the data (dashed) and full multiple scattering fit (solid) for the Pt foil (A), S3 (B), S2 (C), and S1 (D). All the data were measured at 200 K.
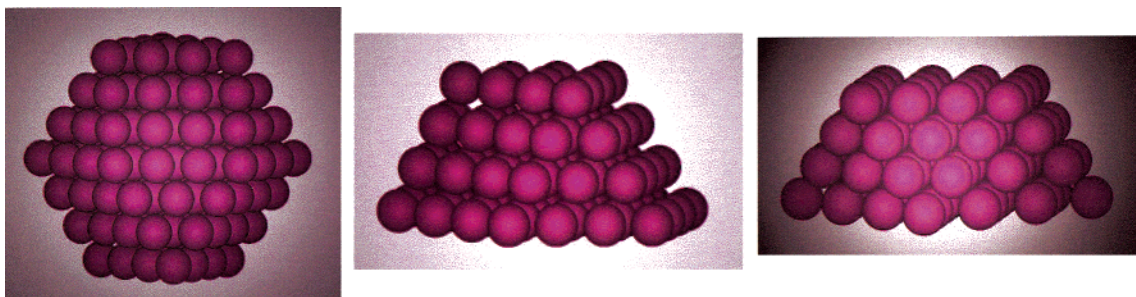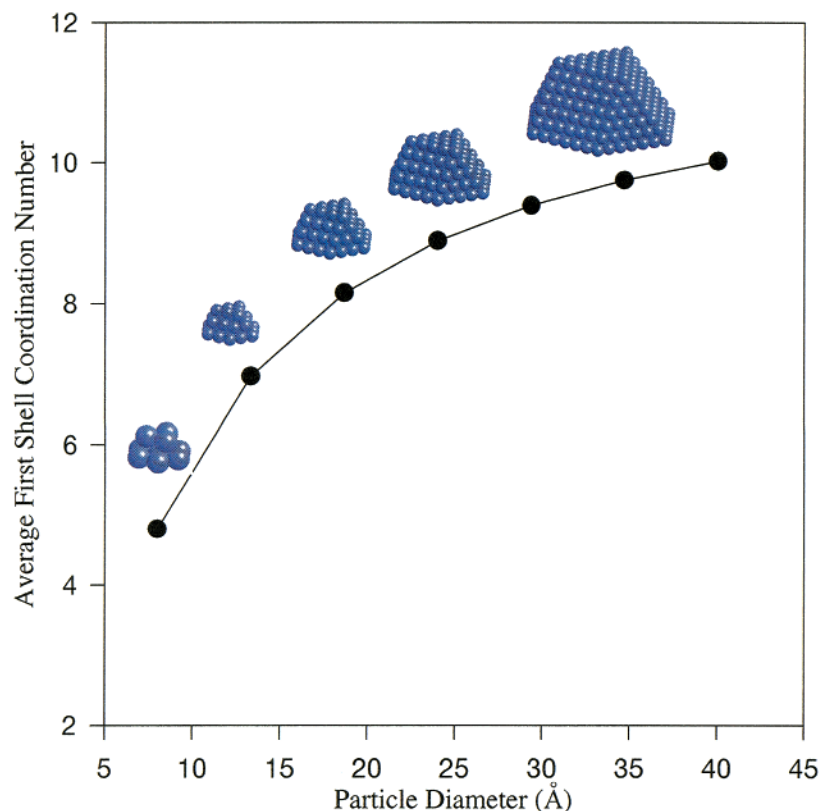
Feature Article

J. Phys. Chem. B, Vol. 105, No. 51, 2001 **12699**

Figure 9. Different models of nanoparticles with $L = 3$ cluster order: (A) cuboctahedron, (B) hemispherical cuboctahedron with a (111) basal plane, and (C) hemispherical cuboctahedron with a (001) basal plane.

SCHEME 3

an unique sequence $\{N_i\}$ of average coordination numbers in the first few nearest-neighbor shells. If such a sequence is obtained experimentally, the corresponding cluster size, shape, and symmetry may be reliably determined. From our EXAFS analysis, the coordination numbers of Pt nanoparticles with different average sizes (S1−S3) were obtained for the first through fifth coordination shells. The atomic packing structure was confirmed to be face centered cubic (fcc) by both electron microdiffraction and EXAFS analyses. The question which remains to be answered is the following. Can we experimentally distinguish between spherical and hemispherical cluster shapes? The following analysis suggests that the answer is yes. We start by comparing the experimentally determined coordination numbers against two models (spherical and hemispherical) that generate quite different sequences of $\{N_i\}$ that we will be able to discriminate against. If the shape-sensitive modeling scheme proves reliable, then further structural refinement can be attempted. This same step also provides a reliable estimate of the particle size, which in turn can be directly compared with the STEM data.

The average coordination numbers for the first through fifth coordination shells were calculated for fcc clusters of three types: (1) a perfect (spherical) cuboctahedron; (2) a half ("hemispherical") cuboctahedron, truncated by a (111) plane; and (3) a half ("hemispherical") cuboctahedron truncated by a (001) plane (Figure 9). The two latter structures are used to distinguish between two possible low-index surface orientations of the nanoparticles relative to the carbon support. The sequences $\{N_i\}$ of average coordination numbers in the first five nearest-neighbor shells were calculated for all cluster orders L (defined here as the number of crusts around the central atom in a cuboctahedron), from $L = 1$ through $L = 15$. Finally, the experimental values and their uncertainties were compared against the model structure. The results of this comparison are shown in Figure 10, which plots the cluster size and shape determination procedure for the smallest particle size (the 24 Å average diameter S1 sample). It is immediately obvious that the (001) truncation model is the least reliable of the three models, since the sequence of experimentally determined coordination numbers $\{N_i\}$ does not lead to an unambiguous
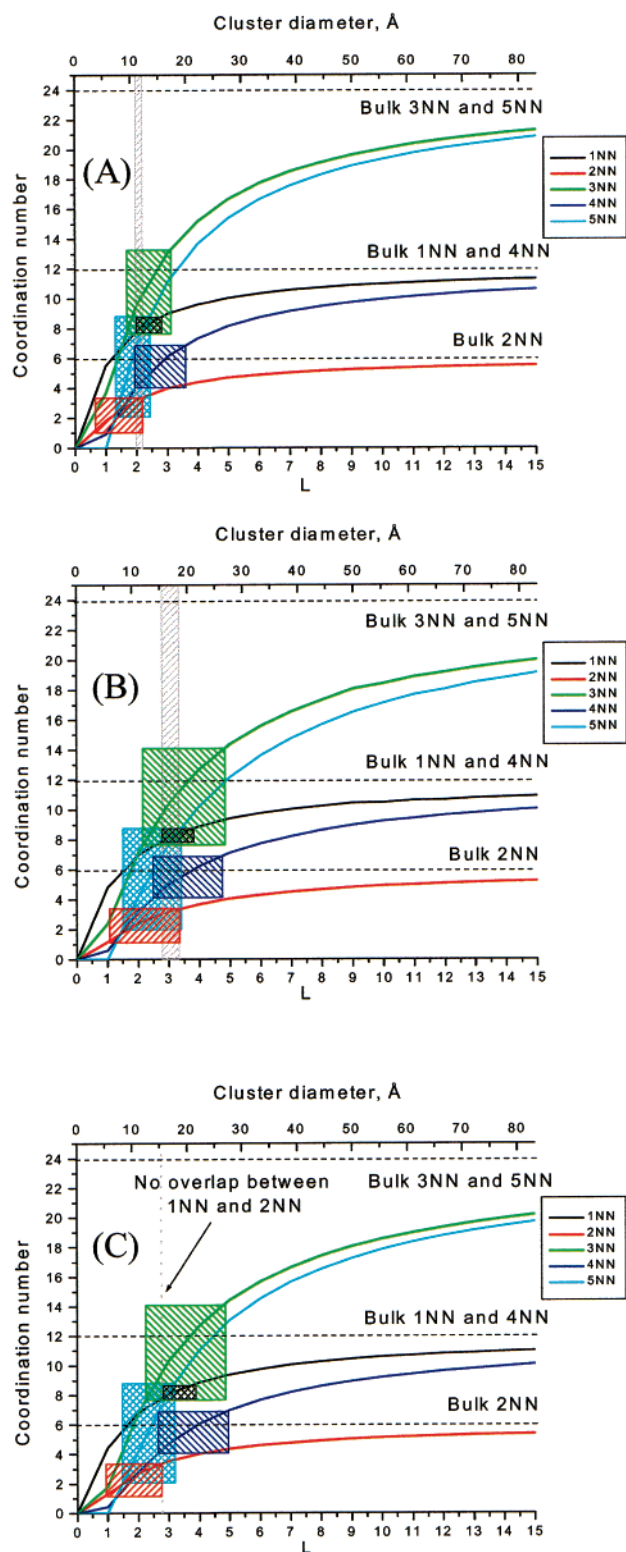
Figure 10. Cluster shape determination: comparison of the average distances (up to 5NN), together with their error bars, measured by EXAFS for the S1 sample and those predicted from the models A−C for various cluster sizes.

cluster size (note: the coordination numbers for the 1NN and 2NN show no overlap to within their uncertainties). The spherical cuboctahedron produces a particle whose diameter (ca. 12 Å) is smaller than the value measured by STEM (24 ± 11 Å). The (111)-truncated hemispherical cuboctahedron provides the best approximation, with a particle size (ca. 17 Å) that is

consistent with that obtained by microscopy and for which a self-consistent overlap of the multi-shell fit exists with the calculated $\{N_i\}$ modula. This same procedure can be applied to the other samples. Assuming the hemispherical (111)-truncated shape found for the S1 sample, the average particle diameters in the S2 and S3 samples were found to be 45 and 78 Å, respectively, results in good agreement with those derived from the microscopy data (Table 1).

Particle Size Effects. It is known that both the physical and chemical properties of small clusters are often different from those of the bulk material.[23] While it is obvious that the cluster properties become increasingly bulklike as the cluster sizes increase, specific structural effects can arise, ones that are determined by size-sensitive perturbations of the electronic structure or the nature and range of the interatomic interactions. We consider here one special example, namely, bond relaxation effects that might give rise to a size-dependent scaling of the clusters metal−metal bond lengths.[24,85−91,94−96] The mechanism of this effect has remained poorly understood to this point. The character of this structural effect may be quantified experimentally for the Pt nanoparticles by studying in an analytical way the size-dependent scaling of the lattice parameters, coordination numbers, and Debye−Waller factors.[97] It is known that the rate at which cluster properties of this sort converge to a bulklike state is a strongly material sensitive property, for example, being fast for ionic clusters[98] and slow for van der Waals rare gas clusters.[99] This convergence rate should also be strongly influenced by the nature of the interatomic interactions that occur between the cluster and support (a feature that unfortunately remains poorly understood in systems of the sort considered here).[100−103]

EXAFS is an ideal probe for structural effects of this sort, since it directly measures short-range atomic structure. In addition, perturbations to the electronic structure associated with the particle size can also be observed in XANES measurements, since the energy of the X-ray absorption edge is directly related to the electronic binding energy of the absorbing atom. The first-principles theories aimed at explaining the mechanisms of size-dependent structural effects, therefore, can be directly compared with the results of EXAFS and XANES experiments and in this way provide a directed basis for their further refinement.

Particle Size Effect on the Electronic Structure. In an earlier study of very small ($\sim$1.5 nm) carbon supported PtRu$_5$ nanoparticles, we found that, upon the reduction of the molecular precursors, the Pt L$_3$-edge position shifted to lower energies by ca. 1.5 eV. Even at this size, the binary clusters exhibit a bulklike energy position of the Pt metal absorption edge, demonstrating that the particles had become completely reduced and metallic in character.[51] The white-line intensity (which characterizes the electronic density of unoccupied d states) also approached that of a Pt metal foil again suggesting an approach to a bulklike limit.

The Pt L$_3$ XANES measurements described in the present work were performed with fully reduced nanoparticles. Therefore, if any of the nanoparticles (e.g., those with a limiting diameter of $\sim$24 Å for the S1 sample) exhibit size-related perturbations in their electronic properties, these should be manifested in the XANES data as both an increase in the white line intensity and a positive shift in the absorption edge position relative to bulk Pt metal. Figure 4 shows the XANES data for our Pt clusters (aligned in absolute X-ray energy and normalized by the absorption edge jump) along with that for a reference Pt metal foil. The spread in the positions of the absorption edge
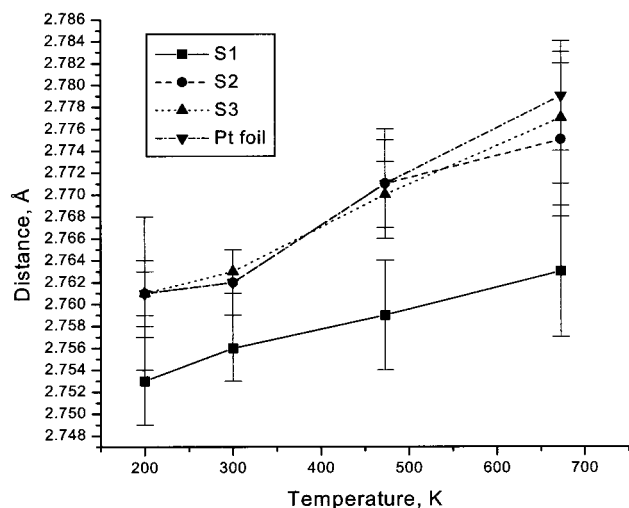
Feature Article

J. Phys. Chem. B, Vol. 105, No. 51, 2001 **12701**

Figure 11. 1NN distances obtained by EXAFS for all particle sizes and the reference Pt foil for different temperatures.

measured for all four samples at four different temperatures is less than 0.2 eV, a value well within the accuracy of our energy alignment procedure. In addition, little change is noted in the intensity of the white line as well. Therefore, the Pt nanoparticles studied in this work all have a metal-like density of d states.

Particle Size Effect on the Lattice Parameter of Supported Pt Nanoclusters. The contraction of lattice constants in metal nanoparticles relative to those expected for bulk samples was first reported in 1951.[85] In this work, a marked lattice contraction in small gold clusters was observed by transmission electron microscopy and later interpreted in terms of surface stress.[86] Another microscopy study of this phenomenon was reported for Al clusters supported on MgO.[87] By analyzing moiré fringe patterns, these investigators were able to characterize an intracluster decrease of lattice parameter of ca. 0.5% that varies progressively from the center toward the surface of the particles. Using an essentially liquid drop model, these effects were interpreted as following directly from an increase in the surface stress due to the high curvature of the particle.

These studies not withstanding, it remains unclear whether small cluster sizes necessarily lead to a contraction of the lattice parameters from a bulklike value. For example, several studies of supported Pd nanoparticles reported that the lattice constant in fact expanded as the particle size decreased.[88] These observations were variously explained as reflecting a pseudomorphism and/or the incorporation of impurities (oxygen, carbon, and hydrogen) into the Pd lattice.[89] Lamber et al.,[90] using electron diffraction to probe Pd nanoclusters, however, found that this material does in fact exhibit a contraction in the lattice constants as the particle size decreases.

Our EXAFS results (Table 3 and Figure 11) clearly reveal that a reduction in the average cluster size leads to a corresponding reduction in the average 1NN interatomic distances (and, therefore, in the lattice parameter as well). As illustrated by the data shown in Figure 11, the average 1NN distance contracts from the bulk value by ca. 0.008(4) Å at 200 K for the smallest S1 (24 Å) particles. Both the larger S2 and S3 particles as well as the bulk Pt have the same value of the 1NN distances of 2.761 Å. The latter observation suggests that the convergence toward a bulklike lattice parameter is rapid for Pt.

Particle Size Effects on Phase Dynamics: Cluster Surface Relaxation. A concurrent, multiple-data-set, first-shell data analysis allows the direct calculation of the 1NN distances along with their static and dynamic disorder (these values are

summarized in Tables 2 and 3). The fact that we obtain a varying nonzero value for the static disorder term, σ_s^2, for the 1NN bond lengths in the nanoparticles, indicates that a size-dependent static disorder exists in the atomic positions (i.e., the atoms do not occupy ideal fcc positions). Indeed, if the only structural disorder present in the lattice were thermal in origin, then the total disorder, σ^2 (eq 3), would be described by the dynamic term only (eq 4), and the static term, σ_s^2, would be zero. In the case of the bulk Pt foil, the value of σ_s^2 obtained (0.0005 Å^2) is below the statistical uncertainty level of the measurement (Table 2). In the nanoparticles, however, the static disorder is seen to increase markedly with the decreasing particle size (Table 2), reaching a maximum value of 0.0017 Å^2 for sample S1. One of the most plausible explanations for the static disorder found in the nanoparticles is the relaxation of the bond lengths exhibited by surface atoms, a process driven by the substantial surface tension of a high radius of curvature solid.[86,87] In response to this compressive tension, the atomic positions of the surface atoms should shift away from ideal fcc sites and toward the cluster's core. Therefore, absent other effects, these surface atoms should have shorter 1NN distances.

To help the reader visualize this effect, we constructed models of clusters exhibiting relaxations limited to two structural cases: (1) bond relaxations that extend throughout the cluster and (2) ones limited to the atoms residing at the surface of the cluster. We specifically note that the models developed here are intended to serve only as a visualization aid and do not follow from the application of a rigorous theoretical treatment. The latter is beyond the scope of this report and will be described elsewhere.[104] The crude models described below do serve quite well, however, to establish the general trends that would be expected in a cluster-size-dependent scaling of the static disorder for the two limiting structural models of that effect.

Using Cerius^2 software (Molecular Simulations, Inc.), models were constructed of hemispherical, (111)-oriented Pt clusters with edge-lengths of $L = 3$ and 8. In the initial configuration, all atoms were held at ideal fcc sites, with a lattice parameter of 3.92 Å. For the first case, we then allowed the surface atoms to relax, using the Universal force field (UFF)[105] to guide that relaxation, while holding the positions of the cluster core atoms fixed. The final atomic positions were then evaluated and the 1NN bond lengths distributions caluclated. We repeated the procedure iteratively, by varying the lattice parameter, until both the average 1NN distance and the static disorder term, σ_s^2, agreed with the experimental results. The most critical point to note from this exercise, despite the limitations of the calculations used to generate the model, is that a surface relaxation always serves to increase the breadth of the distribution of bond distances present. If a sample starts with a finite value for this disorder (e.g., the value of $\sigma_s^2 \approx 0.0005$ Å^2 measured for the bulk Pt sample), relaxation based on a surface contraction mechanism will always lead to an increase in this parameter.

The second model of the relaxation we constructed leads to a very different outcome. A progressive relaxation that radiates to the core of the cluster does not generate a convergent simulation of the bond length static disorder. These distributions, for any physically reasonable limit of the bond length contractions, lead to distributions that are much narrower than those established directly by experiment. Taken together, the molecular graphics analysis offers a very strong suggestion that the relaxation effects that yield the bond-length distributions established by experiment must arise by a mechanism in which these effects are inhomogeneously manifested throughout the cluster. A surface relaxation model appears to be the one that
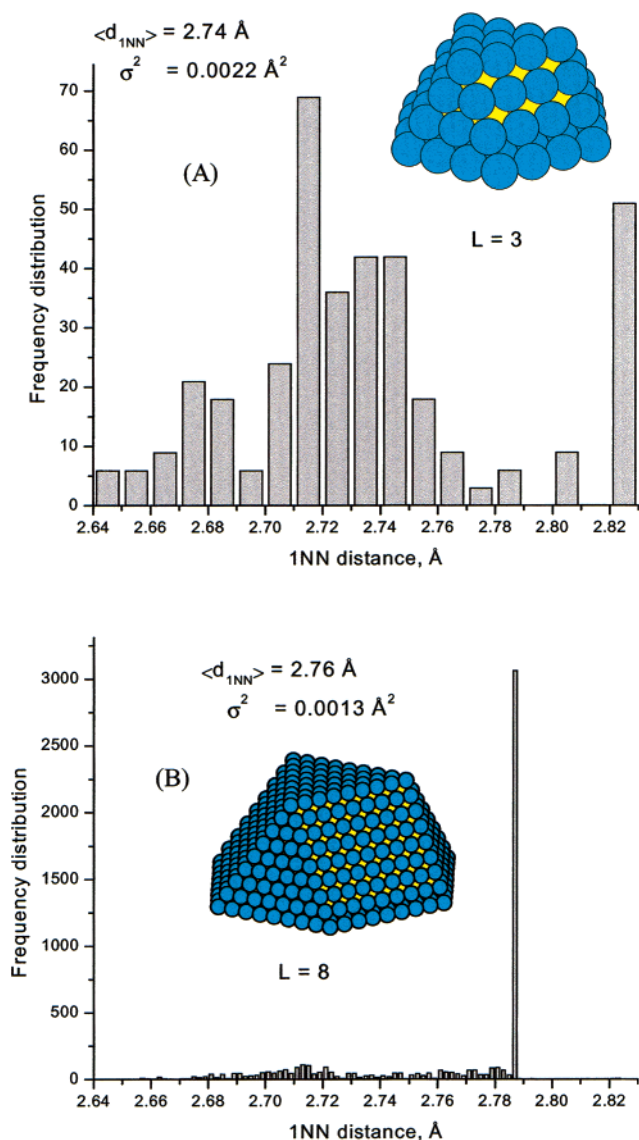
Figure 12. Frequency distribution of the bond lengths over model clusters, as produced by the computer simulation. The clusters were hemispherical cuboctahedra with $L = 3$ (A) and 8 (B), all with the (111) basal plane orientation. The surface atoms were allowed to relax while the bulk atoms were fixed at the periodic fcc sites as described in the text.

is most consistent with the effects measured experimentally, but detailed theoretical models will be needed to definitively establish this point.

The bond length distributions produced for clusters of both $L = 3$ and 8, which correspond to the particle sizes in the samples S1 and S2, respectively, are shown in Figure 12. For the L = 3 cluster, the fraction of the 1NN bonds connecting surface atoms with other atoms (either surface or core) to the total number of 1NN bonds is large (69%). An interesting suggestion is seen in this model. The relaxed surface atoms form shorter 1NN bonds than the average value measured for the cluster. Given that the centroid of the distribution is constrained mathematically to be the average 1NN distance for the cluster measured in the EXAFS experiment, the measured static disorder thus defines the average weighting of other bond lengths that must contribute to this distribution. For the surface relaxation model, then, a convergence to the experiment requires moments in the distribution that lie at distances that are substantially larger ($\sim$2.825 Å for the S1 cluster) than both the

average and the surface bond distances (2.74 and 2.73 Å, respectively). A qualitatively similar trend was observed for the $L = 8$ cluster, although the weighting of "anomalous" bond distances, as expected, is much less pronounced than was the case for the smaller cluster. We are not completely certain what weight to give this latter inference. A mechanism involving compensating motions of atoms does seem to follow from a simple notion that the density of the cluster is partially conserved in the relaxation. If so, then a more complex model of the strain patterns might ultimately need to be considered.

Recognizing that the real picture of how structural relaxations evolve is clearly a complicated one, thorough quantum-level modeling will be needed to shed further light on the inferences developed above. With our colleagues, we hope to report soon on first-principle models that speak directly to this latter need.

Supporting Information Available: Reproducibility test in *k*-space, FT magnitudes of the data and theoretical fit of the PT foil data and S1 data, and temperature-dependent changes in the carbon-supported PT nanoparticles. This material is available free of charge via the Internet at http://pubs.acs.org.

References and Notes

(1) Whitesides, G. M.; Ismagilov, R. F. *Science* **1999**, *284*, 89.
(2) Freeman, W. J.; Kozma, R.; Werbos, P. J. *Biosystems* **2001**, *59*, 109.
(3) Santoli, S. *Acta Astronom.* **2000**, *46*, 641.
(4) Westerhoff, H. V.; Jensen, P. R.; Snoep, J. L.; Kholodenko, B. N. *Thermochim. Acta* **1998**, *309*, 111.
(5) Nederbragt, H. *J. Theor. Biol.* **1997**, *184*, 151.
(6) Craver, C. F. *Philos. Sci.* **2001**, *68*, 53.
(7) Chou, K. C.; Zhang, C. T.; Maggiora, G. M. *Biopolymers* **1994**, *34*, 143.
(8) Lowe, C. R. *Curr. Opin. Struct. Bio.* **2000**, *10*, 428.
(9) Boulas, P. L.; Gomezkaifer, M.; Echegoyen, L. *Angew. Chem., Int. Ed. Engl.* **1998**, *37*, 216.
(10) Gust, D.; Moore, T. A.; Moore, A. L. *J. Photochem. Photobiol., B* **2000**, *58*, 63.
(11) Albrecht, M. *J. Inclusion Phenom. Mol. Recognit. Chem.* **2000**, *36*, 127.
(12) Asefa, T.; Yoshina-Ishii, C.; MacLachlan, M. J.; Ozin, G. A. *J. Mater. Chem.* **2000**, *10*, 1751.
(13) Louloudi, M.; Deligiannakis, Y.; Hadjiliadis, N. *J. Inorg. Biochem.* **2000**, *79*, 93.
(14) Wong, K. K. W.; Mann, S. *Curr. Opin. Colloid Sci.* **1998**, *3*, 63.
(15) Degiorgi, L. *Rev. Mod. Phys.* **1999**, *71*, 687.
(16) Schlottman, P. *Int. J. Mod. Phys. B* **1997**, *11*, 355.
(17) Bulgac, A.; Do Dang, G.; Kusenezov, D. *Phys. A* **2001**, *9*, 429.
(18) Ortiz, G.; Aligia, A. A. *Phys. Status Solidi B* **2000**, *220*, 737.
(19) Jaeger, H. M.; Nagel, S. R.; Behringer, R. P. *Rev. Mod. Phys.* **1996**, *68*, 1259.
(20) Ottino, J. M.; Khakhar, D. V. *Annu. Rev. Fluid Mech.* **2000**, *32*, 55.
(21) Alivisatos, A. P. *J. Phys. Chem.* **1996**, *100*, 13226.
(22) Bradley, J. S. In *The Chemistry of Transition Metal Colloids*; Bradley, J. S., Ed.; VCH: Weinheim, 1994.
(23) In *Nanomaterials: Synthesis, Properties and Applications*; Edelstein, A. S., Cammarata, R. C., Eds.; Institute of Physics Publishing: Bristol, 1998.
(24) El-Sayed, M. A. *Acc. Chem. Res.* **2001**, *34*, 257.
(25) Moriarty, P. *Rep. Prog. Phys.* **2001**, *64*, 297.
(26) Murray, C. B.; Kagan, C. R.; Bawendi, M. G. *Annu. Rev. Mater. Sci.* **2000**, *30*, 545.

Feature Article

J. Phys. Chem. B, Vol. 105, No. 51, 2001 **12703**

(27) Rao, R. C. N.; Giridhar, U.; Thomas, P. J.; Edwards, P. P. *Chem. Soc. Rev.* **2000**, *29*, 27.

(28) Schmid, G.; Baumle, M.; Geerkens, M.; Helm, I.; Osemann, C.; Sawitowski, T. *Chem. Soc. Rev.* **1999**, *28*, 179.

(29) Toshima, N.; Yonezawa, T. *New J. Chem.* **1998**, *22*, 1179.

(30) Aiken, J. D.; Finke, R. G. *J. Mol. Catal. A* **1999**, *145*, 1.

(31) Collier, P. J.; Iggo, J. A.; Whyman, R. *J. Mol. Catal. A* **1999**, *146*, 149.

(32) Croce, F.; Curini, R.; Martinelli, A.; Persi, L.; Ronci, F.; Scrosati, B.; Caminiti, R. *J. Phys. Chem. B* **1999**, *103*, 10632.

(33) Huang, X. H.; Huang, H. Z.; Wu, N. Z.; Hu, R. S.; Zhu, T.; Liu, Z. F. *Surf. Sci.* **2000**, *459*, 183.

(34) Johnson, B. F. G. *Coordin. Chem. Rev.* **1999**, *192*, 1269.

(35) Leslie-Pelecky, D. L.; Zhang, X. Q.; Kim, S. H.; Bonder, M.; Rieke, R. D. *Chem. Mater.* **1998**, *10*, 164.

(36) Yu, E. T. *Mater. Sci. Eng. R* **1996**, *17*, 147.

(37) Zou, S. Z.; Villegas, I.; Stuhlman, C.; Weaver, M. J. *Electrochim. Acta* **1998**, *43*, 2811.

(38) Aiken, J. D.; Finke, R. G. *Chem. Mater.* **1999**, *11*, 1035.

(39) Biffis, A.; Zecca, M.; Basato, M. *Eur. J. Inorg. Chem.* **2001**, *5*, 1131.

(40) Borsia, A.; Wilhelm, A. M.; Delmas, H. *Catal. Today* **2001**, *66*, 389.

(41) Kralik, M.; Corain, B.; Zecca, M. *Chem. Pap.—Chem. Zvesti* **2000**, *54*, 254.

(42) Lange, C.; De Caro, D.; Gamez, A.; Storck, S.; Bradley, J. S.; Maier, W. F. *Langmuir* **1999**, *15*, 5333.

(43) Schneider, J. J.; Czap, N.; Hagen, J.; Engstler, J.; Ensling, J.; Gutlich, P.; Reinoehl, U.; Bertagnolli, H.; Luis, F.; de Jongh, L. J.; Wark, M.; Grubert, G.; Hornyak, G. L.; Zanoni, R. *Chem.—Eur. J.* **2000**, *6*, 4305.

(44) Sinfelt, J. H. *Bimetallic Catalysts - Discoveries, Concepts, and Applications*; Wiley: New York, 1983.

(45) Toshima, N.; Shiraishi, Y.; Teranishi, T.; Miyake, M.; Tominaga, T.; Watanabe, H.; Brijoux, W.; Bonneman, H.; Schmid, G. *Appl. Organomet. Chem.* **2001**, *15*, 178.

(46) Gates, B. C. *Chem. Rev.* **1995**, *95*, 5.

(47) Meutterties, E. L.; Rhodin, T. N.; Band, E.; Brucker, C. F.; Pretzer, W. R. *Chem. Rev.* **1979**, *79*, 91.

(48) Meutterties, E. L.; Krause, M. J. *Angew. Chem., Int. Ed. Engl.* **1983**, *22*, 135.

(49) Datye, A. K. *Top. Catal.* **2000**, *13*, 131.

(50) Jefferson, D. A. *Philos. Trans. R. Soc. London, Ser. A* **2000**, *358*, 2683.

(51) (a) Nashner, M. S.; Frenkel, A. I.; Shapley, J. R.; Nuzzo, R. G. *J. Am. Chem. Soc.* **1997**, *119*, 7760. (b) Nashner, M. S.; Frenkel, A. I.; Sommerville, D.; Hills, C. W.; Shapley, J. R.; Nuzzo, R. G. *J. Am. Chem. Soc.* **1998**, *120*, 8093. (c) Hills, C. W.; Nashner, M. S.; Frenkel, A. I.; Shapley, J. R.; Nuzzo, R. G. *Langmuir* **1999**, *15*, 690.

(52) Sayers, D. E.; Lytle, F. W.; Stern, E. A. *Phys. Rev. Lett.* **1971**, *27*, 1204.

(53) Lytle, F. W.; Via, G. H.; Sinfelt, J. H. *J. Chem. Phys.* **1977**, *67*, 3831.

(54) Sinfelt, J. H.; Via, G. H.; Lytle, F. W. *J. Chem. Phys.* **1977**, *68*, 2009.

(55) Via, G. H.; Sinfelt, J. H.; Lytle, F. W. *J. Chem. Phys.* **1979**, *71*, 690.

(56) Sinfelt, J. H.; Via, G. H.; Lytle, F. W. *J. Chem. Phys.* **1980**, *72*, 4832.

(57) Sinfelt, J. H.; Via, G. H.; Lytle, F. W.; Greegor, R. B. *J. Chem. Phys.* **1981**, *75*, 5527.

(58) Sinfelt, J. H.; Via, G. H.; Lytle, F. W. *J. Chem. Phys.* **1982**, *76*, 2779.

(59) Marques, E. C.; Sandstrom, D. R.; Lytle, F. W.; Greegor, R. B. *J. Chem. Phys.* **1982**, *77*, 1027.

(60) Meitzner, G.; Via, G. H.; Lytle, F. W.; Sinfelt, J. H. *J. Chem. Phys.* **1983**, *78*, 882.

(61) Meitzner, G.; Via, G. H.; Lytle, F. W.; Sinfelt, J. H. *J. Chem. Phys.* **1983**, *78*, 2533.

(62) Meitzner, G.; Via, G. H.; Lytle, F. W.; Sinfelt, J. H. *J. Chem. Phys.* **1985**, *83*, 353.

(63) Meitzner, G.; Via, G. H.; Lytle, F. W.; Sinfelt, J. H. *J. Chem. Phys.* **1985**, *83*, 4793.

(64) Meitzner, G.; Via, G. H.; Lytle, F. W.; Sinfelt, J. H. *J. Chem. Phys.* **1987**, *87*, 6354.

(65) Okube, M.; Yoshiasa, A. *J. Synchrotron. Radiat.* **2001**, *8*, 937.

(66) In *X-ray Absorption: Principles, Applications, Techniques of EXAFS, SEXAFS, and XANES*; Koningsberger, D. C., Prins, R., Eds.; Wiley: New York, 1988.

(67) Stern, E. A.; Heald, S. M. In *Handbook on Synchrotron Radiation*; Koch, E. E., Ed.; North-Holland: New York, 1983; Vol. 1.

(68) Greegor, R. B.; Lytle, F. W. *J. Catal.* **1980**, *63*, 476.

(69) Edington, J. W. *Practical Electron Microscopy*; Philips: Eindhoven, The Netherlands, 1975.

(70) Gallezot, P.; Leclercq, C. In *Characterization of Catalysts by Conventional and Analytical Electron Microscopy*; Gallezot, P., Leclercq, C., Eds.; Plenum: New York, 1994.

(71) Rehr, J. J.; Albers, R. C. *Rev. Mod. Phys.* **2000**, *72*, 621.

(72) Zabinsky, S. I.; Rehr, J. J.; Ankudinov, A.; Albers, R. C.; Eller, M. J. *J. Phys. Rev. B* **1995**, *52*, 2995.

(73) Stern, E. A.; Newville, M.; Ravel, B.; Yacoby, Y.; Haskel, D. *Phys. B* **1995**, *208 & 209*, 117.

(74) Filipponi, A.; Di Cicco, A.; Tyson, T. A.; Natoli, C. R. *Solid State Commun.* **1991**, *78*, 265.

(75) The entire list of EXAFS data analysis packages is available on the website of the International XAFS Society, http://ixis.csrri.iit.edu.

(76) Lee, P. A.; Pendry, J. B. *Phys. Rev. B* **1975**, *11*, 2795.

(77) Bunker, G.; Stern, E. A. *Phys. Rev. Lett.* **1985**.

(78) Frenkel, A. I.; Stern, E. A.; Qian, M.; Newville, M. *Phys. Rev. B* **1993**, *48*, 12449.

(79) Frenkel, A. I.; Stern, E. A.; Voronel, A.; Qian, M.; Newville, M. *Phys. Rev. Lett.* **1993**, *71*, 3485.

(80) Frenkel, A. I.; Stern, E. A.; Voronel, A.; Qian, M.; Newville, M. *Phys. Rev. B* **1994**, *49*, 11662.

(81) Tan, Z.; Budnick, J. I.; Heald, S. M. *Rev. Sci. Instrum.* **1989**, *60*, 1021.

(82) Newville, M.; Livins, P.; Yacoby, Y.; Rehr, J. J.; Stern, E. A. *Phys. Rev. B* **1993**, *47*, 14126.

(83) Frenkel, A. I.; Rehr, J. J. *Phys. Rev. B* **1993**, *48*, 585.

(84) *The Handbook of Chemistry and Physics*, 48 ed.; The Chemical Rubber Co.: Cleveland, Ohio, 1967.

(85) Boswell, F. W. C. *Proc. Phys. Soc. (London)* **1951**, *A64*, 465.

(86) Vermaak, J. S.; Mays, C. W.; D., K.-W. *Surf. Sci.* **1968**, *12*, 128.

(87) Woltersdorf, J.; Nepijko, A. S.; Pippel, E. *Surf. Sci.* **1981**, *106*, 64.

(88) (a) Heineman, K.; Poppa, H. *Surf. Sci.* **1985**, *156*, 265. (b) Teranishi, T.; Miyake, M. *Chem Mater.* **1998**, *10*, 594, and references therein.

(89) Goyhenex, C.; Henry, C. R.; Urban, J. *Philos. Mag. A* **1994**, *69*, 1073.

(90) Lamber, R.; Weitjen, S.; Jaeger, N. I. *Phys. Rev. B* **1995**, *51*, 10968.

(91) Kaszkur, Z. *J. Appl. Crystollagr.* **2000**, *33*, 87.

(92) Frenkel, A. I. *J. Synchotron Rad.* **1999**, *6*, 293.

(93) Montejano-Carrizales, J. M.; Moran-Lopez, J. L. *Nanostruct. Mater.* **1992**, *1*, 397.

(94) Marcus, P. M.; Qian, X. H.; Hubner, W. *J. Phys.: Condens. Mater.* **2000**, *12*, 5541.

(95) Tanaka, M.; Makino, Y. *Ferroelectrics Lett.* **1998**, *24*, 13.

(96) Kaszkur, Z. *J. Appl. Crystallogr.* **2000**, *33*, 1262.

(97) Jortner, J. Z. *Phys. D* **1992**, *24*, 247.

(98) Martin, T. P. *Phys. Rep.* **1983**, *95*, 169.

(99) Farges, F.; de Feraudy, M. G.; Raoult, B.; Torchet, G. J. *J. Chem. Phys.* **1983**, *78*, 5067.

(100) Llorca, J.; de la Piscina, P. R.; Fierro, J. G.; Sales, J.; Homs, N. *J. Mol. Catal. A* **1997**, *118*, 101.

(101) Gota, S.; Gautier, M.; Douillard, L.; Thromat, N.; Duraud, J. P.; Le Fevre, P. *Surf. Sci.* **323**, *323*, 163.

(102) Masek, K.; Matolin, V.; Gillet, M. *Thin Solid Films* **1995**, *260*, 252.

(103) Alerasool, S.; Gonzalez, R. D. *J. Catal.* **1990**, *124*, 204.

(104) Khare, S.; Frenkel, A. I.; Hills, C. W.; Johnson, D.; Nuzzo, R. G. Unpublished results.

(105) Rappe, A. K.; Casewit, C. J.; Colwell, K. S.; Goddard, W. A. III.; Skiff, W. M. *J. Am. Chem. Soc.* **1992**, *114*, 10024.